PAPER

Check for updates

Wearable enzyme-free glucose sensor using a flexible sericin-based conductive bio-composite

Xiaorui Huang,†[a] Yi Li,†*[a] Boxiang Yang,†[a] Yuxuan Wu,[a] Zhuocheng Jiang,[a] Jiuxi Sui,[a] Siyi Xing,[a] Xue Zhang,[a] Hualin Lan,[c] Hanyan Zou,*[b] Yuchan Zhang*[a] and Guangchao Zang (ID) *[a]

With over 500 million people affected by diabetes worldwide, there is an urgent need for painless, continuous glucose monitoring. However, current wearable sensors are limited by enzyme instability, mechanical rigidity, and poor correlation with blood glucose levels. Here, we present an eco-friendly flexible biosensor fabricated from silk sericin, an abundant cocoon by-product, crosslinked with dialdehyde HPMC and functionalized with AuNPs–AMWCNTs. This dual-crosslinking strategy integrates sericin's biocompatibility with the high conductivity and catalytic activity of the nanocomposite, yielding a robust sensing layer that withstands 200 folding cycles without performance loss. The sensor exhibits a low detection limit of 4 μM and a sensitivity of 13.43 μA mM^{-1} cm^{-2} in the physiologically relevant 25–400 μM range. This work offers a sustainable and reliable platform for real-time, continuous, and noninvasive glucose monitoring, with significant potential for next-generation wearable health devices.

1. Introduction

With the increasing interest in body health monitoring, new skin biosensors have attracted more attention and improved rapidly in recent years.[1] Among various biosensors and sensing platforms, electrochemical sensors that detect physiological components in sweat and convert them into electronic signals for monitoring life indicators have recently gained much research interest.[2] Many disorders, such as diabetes, can be monitored by analyzing glucose levels in sweat. Sweat glands are distributed across the body; thus, sweat can be collected continuously and noninvasively, which is more convenient than collecting other body fluids. Traditional blood glucose testing by finger-prick is invasive and causes discomfort, highlighting the need for less invasive and more user-friendly approaches such as sweat-based flexible skin sensors.

Flexible skin sensors are typically fabricated from biocompatible materials, which helps reduce skin irritation.[3] In addition, a series of eco-friendly biosensors can be created from natural, biodegradable, and non-toxic materials.[4] Sericin, a natural protein derived from silkworm cocoons, exhibits good biocompatibility, low toxicity, and environmental friendliness.[5] It contains multiple modifiable chemical groups,[6] such as carboxyl, amino, and hydroxyl, giving it great potential for electrochemical detection.[7] Hydroxypropyl methyl cellulose (HPMC) is a water-soluble, biocompatible thickening agent with excellent film-forming ability.[8] It can be selectively oxidized by periodate to produce dialdehyde HPMC (DHMC).[9] Cross-linking sericin with DHMC can theoretically improve its mechanical properties and broaden its application potential.[10] Therefore, sericin and DHMC were chosen as the raw materials in this study to prepare a flexible bio-composite membrane.

Improving the electrical conductivity of biosensors is also essential. Amino-functionalized multi-walled carbon nanotubes (AMWCNTs) are widely used due to their strong catalytic activity.[11] When modified with metal nanoparticles, AMWCNTs provide abundant catalytic sites for glucose oxidation and show minimal toxicity, making them highly suitable for enzyme-free glucose detection.[12] Modifying AMWCNTs with AuNPs further enhances conductivity, dispersibility, and thermal stability.[13]

In this work, we developed a flexible bio-composite film by combining silk sericin (SS), DHMC, and AuNPs–AMWCNTs to achieve excellent biocompatibility and electrocatalytic performance for enzyme-free glucose detection. The Schiff-base crosslinking reaction ensured strong structural integrity, while the AuNPs–AMWCNT network enhanced electron transfer and catalytic efficiency. The film was further integrated onto a screen-printed electrode to construct a wearable platform for

[a] *Biomedical Innovation and Entrepreneurship Practice Base, Lab Teaching & Management Center, Chongqing Medical University, Chongqing, China.*
E-mail: liyicqmu@cqmu.edu.cn, zhangyc@cqmu.edu.cn, zangguangchao@cqmu.edu.cn

[b] *Institute for Food and Drug Control, Chongqing, China.*
E-mail: zouhanyan@cqifdc.org.cn

[c] *Chongqing Quality Testing & Inspection Center for Medical Devices, Chongqing, China*

† These authors contributed equally to this work.

real-time sweat glucose monitoring. This strategy offers a sustainable and reliable approach for continuous, noninvasive glucose sensing, with promising potential for personalized health management.

2. Materials and methods

2.1 Materials and instruments

Silkworm cocoons were obtained from a local sericulture farm in Chongqing, China. Hydroxypropyl methylcellulose (HPMC) was purchased from Tianjin Guangfu Fine Chemical Research Institute. Sodium periodate ($NaIO_4$) and chloroauric acid ($HAuCl_4 \cdot 3H_2O$) were purchased from Shanghai Adamasbeta Co., Ltd. Aminated multi-walled carbon nanotubes (AMWCNTs, purity >95%) were acquired from Nanjing XFNANO Materials Technology Co., Ltd. All other chemicals were of analytical grade and used without further purification.

Cell fluorescence imaging was performed using an Eclipse Ti-U inverted fluorescence microscope (Nikon, Japan), while material surface morphologies and elemental compositions were characterized using an SU8010 field-emission scanning electron microscope (Hitachi, Japan) coupled with an X-MaxN energy-dispersive X-ray spectrometer (Oxford Instruments). X-ray diffraction (XRD) patterns were obtained using a D8 ADVANCE diffractometer (Bruker, Germany). Fourier-transform infrared (FTIR) spectra were collected on an iS50 spectrometer (Nicolet, US) over a wavelength range of 400 to $4000~cm^{-1}$. Electrochemical tests employed a three-electrode system consisting of the conductive composite film as the working electrode (CHI660E, Shanghai, China), an Ag/AgCl (saturated KCl) reference electrode, and a platinum wire counter electrode. All instruments were calibrated according to the manufacturers' standard protocols prior to use.

2.2 Preparation of the sensor

2.2.1 Synthesis of the SS–DHMC composite substrate.
Silkworm cocoons were treated with high-pressure steam (121 °C, 20 min) to extract SS. The extracted SS was lyophilized to obtain purified SS powder. DHMC was synthesized *via* $NaIO_4$ oxidation by reacting 4% (w/v) HPMC (Tianjin Guangfu) with 5.28% (w/v) $NaIO_4$ at pH 3.5 and 40 °C for 5 h. The product was dialyzed and dried at 50 °C. To perform chemical crosslinking, DHMC (0.05 g) was dissolved in 2 mL ultrapure water to create a 2.5% (w/v) solution. SS powder (0.05 g) was added to this solution, and the mixture was stirred at 60 °C for 1 h to form a 3D Schiff base network.

2.2.2 Synthesis of the AuNP–AMWCNT nanocomposite.
Preparation of the AuNP–AMWCNT nanocomposite was performed essentially as described by Chen, *et al.*[14] AMWCNTs (10 mg, Nanjing XFNANO) were dispersed in 10 mL 3% sodium citrate, and the mixture was sonicated and then boiled. Five milliliters of 1% $HAuCl_4$ were added to the mixture until a wine-red color appeared. The product was centrifuged and washed to obtain AuNPs–AMWCNTs.

2.2.3 Assembly of the SS–DHMC–AuNPs–AMWCNT sensor.
The AuNPs–AMWCNT content is reported as v/v, defined as the volume fraction of the stock dispersion in the casting mixture. A pilot screen indicated insufficient percolation and weak redox responses at <5%, whereas >20% produced high slurry viscosity, local agglomeration and poor film integrity. Therefore, 5–20% was selected as a practical optimization window. Sufficient AuNPs–AMWCNT was blended into the SS–DHMC solution to achieve a concentration of 5–20% (v/v), and the mixture was magnetically stirred for 12 h. The mixture was cast onto polydimethylsiloxane molds, dried at 40 °C, and peeled into self-standing films ($1 \times 1~cm^2$) for electrochemical testing (Fig. 1).

2.3 Biocompatibility evaluation

2.3.1 Cytotoxicity assay.
L929 cells (iCell Bioscience, Shanghai) and HeLa-RFP cells (Mingzhou Biotechnology, Ningbo) were cultured in DMEM with 10% FBS and 1% penicillin–streptomycin at 37 °C in a 5% CO_2 atmosphere. The CCK-8 assay (Fisher Scientific, USA) was performed after 24 h of culture in the presence of film samples ($0.3 \times 0.3~cm^2$). The absorbance was measured at 450 nm.

2.3.2 Histological analysis.
Sprague Dawley rats (200 ± 20 g, specific pathogen-free grade) were acclimatized for 1 week (23 ± 1 °C, 50 ± 5% humidity, 12/12 h light–dark cycle) prior to subcutaneous implantation of composite film samples under isoflurane anesthesia. On day 7 following implantation, the rats were sacrificed, and the major organs were harvested. Tissue sections (5 μm) were stained with hematoxylin and eosin (H&E) to evaluate inflammatory responses. All animal procedures were performed in accordance with the Guidelines for Care and Use of Laboratory Animals of Chongqing Medical University and approved by the Institutional Animal Ethics Committee (Approval No.: IACUC-CQMU-2024-0490) and AAALAC guidelines.

2.4 Electrochemical characterization of conductive composite films

The area (1 cm × 1 cm) of composite films with distinct films was detected by CV from −0.55 V to 0.65 V at a scan rate of 100 mV s^{-1} in a 0.1 mM pH = 7.0 PBS solution and electrochemical impedance spectroscopy (EIS) in a 0.05 M KCl solution containing 0.5 mM $[Fe(CN)_6]^{3-/4-}$. In a stationary solution, linearity tests for DPV and CV were performed. The DPV method was used to examine several interfering chemicals. The anti-jamming ability was assessed by comparing the current value before and after the addition of various interferents.

3. Results and discussion

3.1 Physical and chemical characterization of SS–DHMC–AuNPs–AMWCNTs

Comprehensive analyses that employ multiple characterization techniques can reveal key information regarding chemical composition, microstructure, crystal
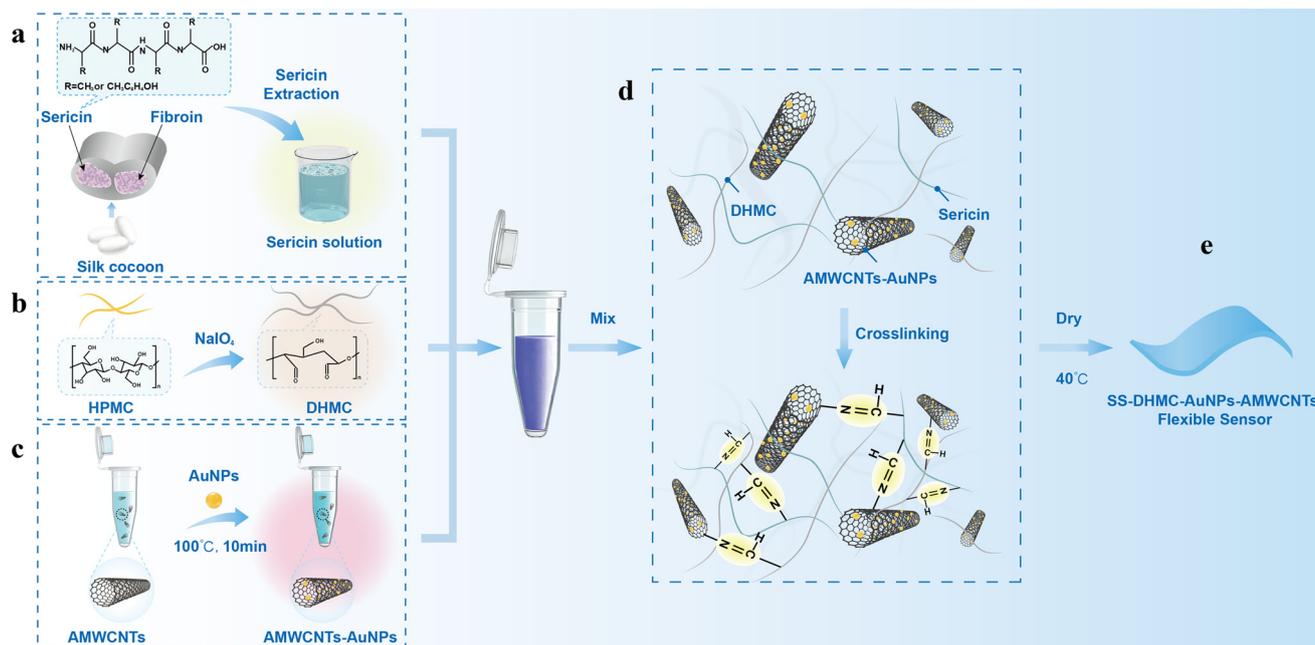
Fig. 1 Schematic illustration of the process of fabrication of SS–DHMC–AuNPs–AMWCNTs. (a) Extraction of sericin; (b) oxidation of hydroxypropyl methylcellulose (HPMC) to produce dialdehyde hydroxymethyl cellulose (DHMC); (c) synthesis of gold nanoparticles (AuNPs)–AMWCNTs; (d) mixing to establish crosslinking between components; (e) drying to obtain the SS–DHMC–AuNPs–AMWCNT flexible electrode.

structure, and elemental distribution.[15] In this study, systematic characterization of the SS–DHMC–AuNPs–AMWCNT composite film was used to verify the preparation of the material and to provide a theoretical foundation for understanding its performance advantages.

First, the crosslinking state of the composite film was analyzed by FT-IR spectroscopy (Fig. 2a). Oxidation of HPMC with NaIO$_4$ led to the appearance of an absorption peak at 1730 cm^{-1} that is not present in the reported spectrum of HPMC.[16] This peak was attributed to aldehyde carbonyl vibration, and its presence is consistent with the formation of DHMC. However, the absorption spectrum of SS–DHMC showed no peak at 1730 cm^{-1}, indicating that the aldehyde groups had undergone chemical reactions in the presence of SS.[17] The characteristic vibration peak of the Schiff base C=N bond (around 1660 cm^{-1}) was not observed in SS–DHMC, likely due to masking by the amide I band (1600–1690 cm^{-1}) of SS.[18] After crosslinking, the FT-IR spectrum of SS–DHMC–AuNPs–AMWCNTs was consistent with a slight transformation in the secondary structure of SS, from random coil to α-helix.[19]

XRD analysis (Fig. 2b) was used to investigate the crystal structure of the material. The peaks in the spectrum of SS–DHMC–AMWCNTs at 25.85° and 42.6° were attributed to the (002) and (100) crystal planes of AMWCNTs,[20] while the newly emerged diffraction peaks of SS–DHMC–AuNPs–AMWCNTs at 38.15°, 44.35°, 64.6°, 77.6°, 81.9°, 110.85°, and 115.3° were assigned to the (111), (200), (220), (311), (222), (331), and (422) crystal planes of AuNPs, respectively.[21] The appearance of these characteristic peaks confirmed the successful loading of AuNPs–AMWCNTs, and this indicated the

presence of numerous high-index crystal planes that could increase the surface energy relative to free AuNPs,[22] thereby enhancing the material's reactivity and amenability to use in electrochemical detection.

We next performed SEM analysis of the to investigate the microstructure of the composite film, as microstructure is key to the performance of any material. As shown in Fig. 2c, the SS–DHMC–AuNPs–AMWCNT film exhibited a uniform porous structure, suggesting that the material has a relatively high specific surface area and capacity for efficient mass transfer.[23] The microporosity might also increase the number of electrochemically active sites,[24] greatly facilitating subsequent electrochemical detection.

An elemental quantitative analysis (Fig. 2d) confirmed that the proportions of C, O, and Au were consistent with expectations, accounting for 19.52%, 55.73%, and 23.82%, respectively, of the total mass of the material, providing quantitative evidence for the composition of the composite. EDS mapping (Fig. 2e) showed that Au was uniformly dispersed in the material, indicating no significant aggregation of AuNPs, with most nanoparticles having a diameter of 50 nm, further increasing the surface area of the porous structure.[25]

The stability of the material is a key factor determining its practical applicability as a flexible sensor substrate.[26] We found that the SS–DHMC–AuNPs–AMWCNT film maintained its structural integrity after immersion in water, with no noticeable damage or detachment of the AuNPs (Fig. 2f). This stability likely stems from the covalent crosslinked network formed between SS and DHMC, which provides a robust framework, and the incorporation of AMWCNTs,
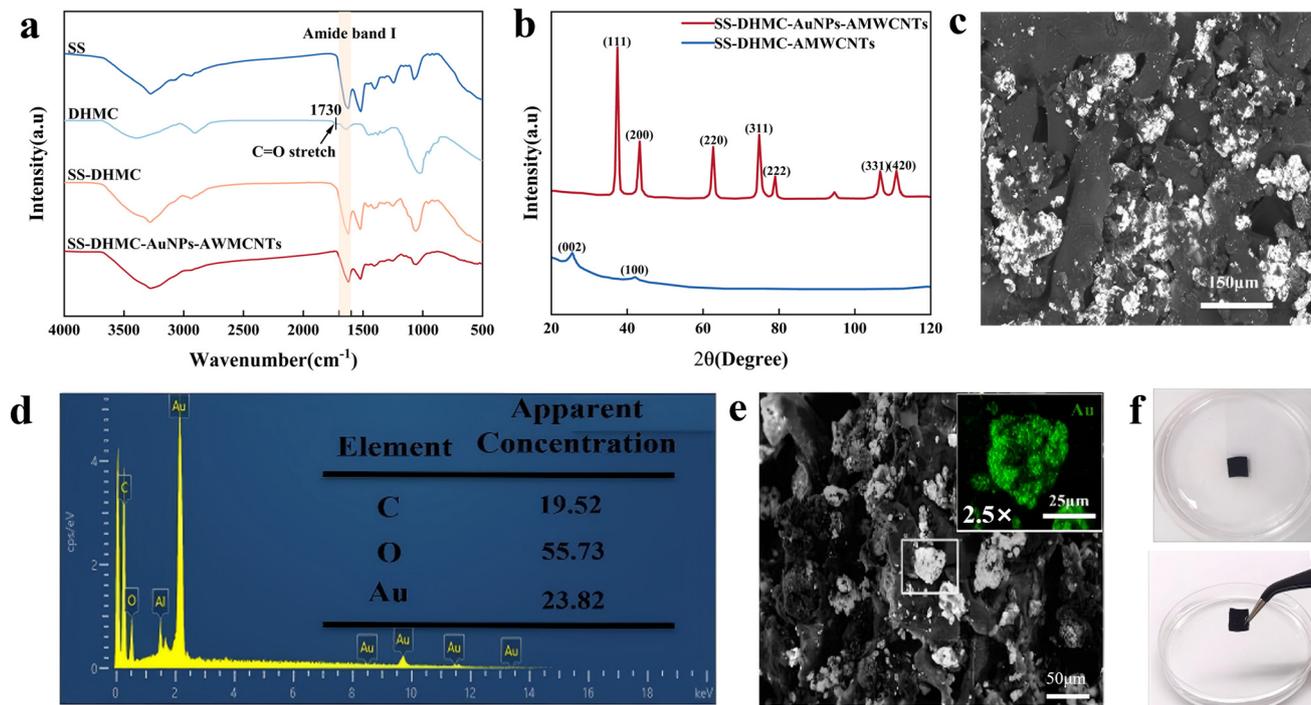
Fig. 2 Physical and chemical characterization of the SS–DHMC–AuNPs–AMWCNT film. (a) FT-IR spectra of SS, DHMC, SS–DHMC, and SS–DHMC–AuNPs–AMWCNTs; (b) XRD patterns of the SS–DHMC–AMWCNT film and SS–DHMC–AuNPs–AMWCNTs; (c) representative SEM image of SS–DHMC–AuNPs–AMWCNTs; (d) elemental composition of the SS–DHMC–AuNPs–AMWCNT composite film; (e) EDS spectrum of SS–DHMC–AuNPs–AMWCNTs, 2.5× magnification in the upper right corner (with energy spectrum of Au); (f) structural stability of the SS–DHMC–AuNPs–AMWCNT film after immersion in water.

which enhances the mechanical strength of the material.[14,27] Moreover, it's swelling rate in water remained around 2.15 after 96 hours and tended to stabilize, which has favourable and stable water absorption (Fig. S1).

Compared to traditional polymer-based composites,[28] the composite material prepared in this work exhibits significantly better stability while maintaining a well-defined structure. We attribute this improvement primarily to the multi-level crosslinking strategy employed in the material design, as Schiff base reactions are known to form a stable covalent network at the molecular level.[29] In addition, the interactions between AuNPs–AMWCNTs and the matrix at the nanoscale further enhance structural stability.[30] Not only do the uniformly dispersed AuNPs provide abundant active sites, but they may also synergistically improve the conductivity of the material conductivity through interactions with AMWCNTs.[31]

In summary, systematic characterization confirmed the successful preparation of the SS–DHMC–AuNPs–AMWCNT composite film, and it also provided important insights into its structure–performance relationship. The excellent stability demonstrated by this material lays a solid foundation for its practical application in sensor technologies, particularly for sensing systems that require long-term stability. Further research is needed to determine and optimize the long-term stability of the material under various environmental conditions and to establish quantitative relationships between its sensing performance and microstructure.

3.2 Biocompatibility of the composite materials

Biocompatibility is a critical parameter when evaluating the potential clinical applicability of biomedical materials.[32,33] In this study, we systematically investigated the biocompatibility of the SS–DHMC–AuNPs–AMWCNT composite through both *in vitro* cell experiments and *in vivo* animal experiments (Fig. 3). *In vitro*, both SS–DHMC–AMWCNTs and SS–DHMC–AuNPs–AMWCNTs exhibited excellent cytocompatibility in comparison with the control treatment. Specifically, fluorescence microscopy analyses (Fig. 3a) demonstrated that HeLa cells adhered with higher cell densities onto both composite surfaces as compared with a control surface, and the adhered cells exhibited an apparently normal morphology. When L929 cells were incubated in the presence of SS–DHMC–AMWCNTs and SS–DHMC–AuNPs–AMWCNTs, the proliferation rates relative to control were found by the CCK-8 assay to be 106.5% and 109.4%, respectively (Fig. 3b). Similar results were observed for other research, in which the microporous structure was demonstrated to be directly responsible for increased adhesion of the cell.[34] Taken together, these results indicated an apparent lack of cytotoxicity and suggested that the porous structure of the material might promote cell adhesion and proliferation.

To evaluate the potential safety of epidermal biosensors created from the material, three composite films (SS–DHMC, SS–DHMC–AMWCNTs and SS–DHMC–AuNPs–AMWCNTs) were implanted subcutaneously in the dorsal skin of rats. All
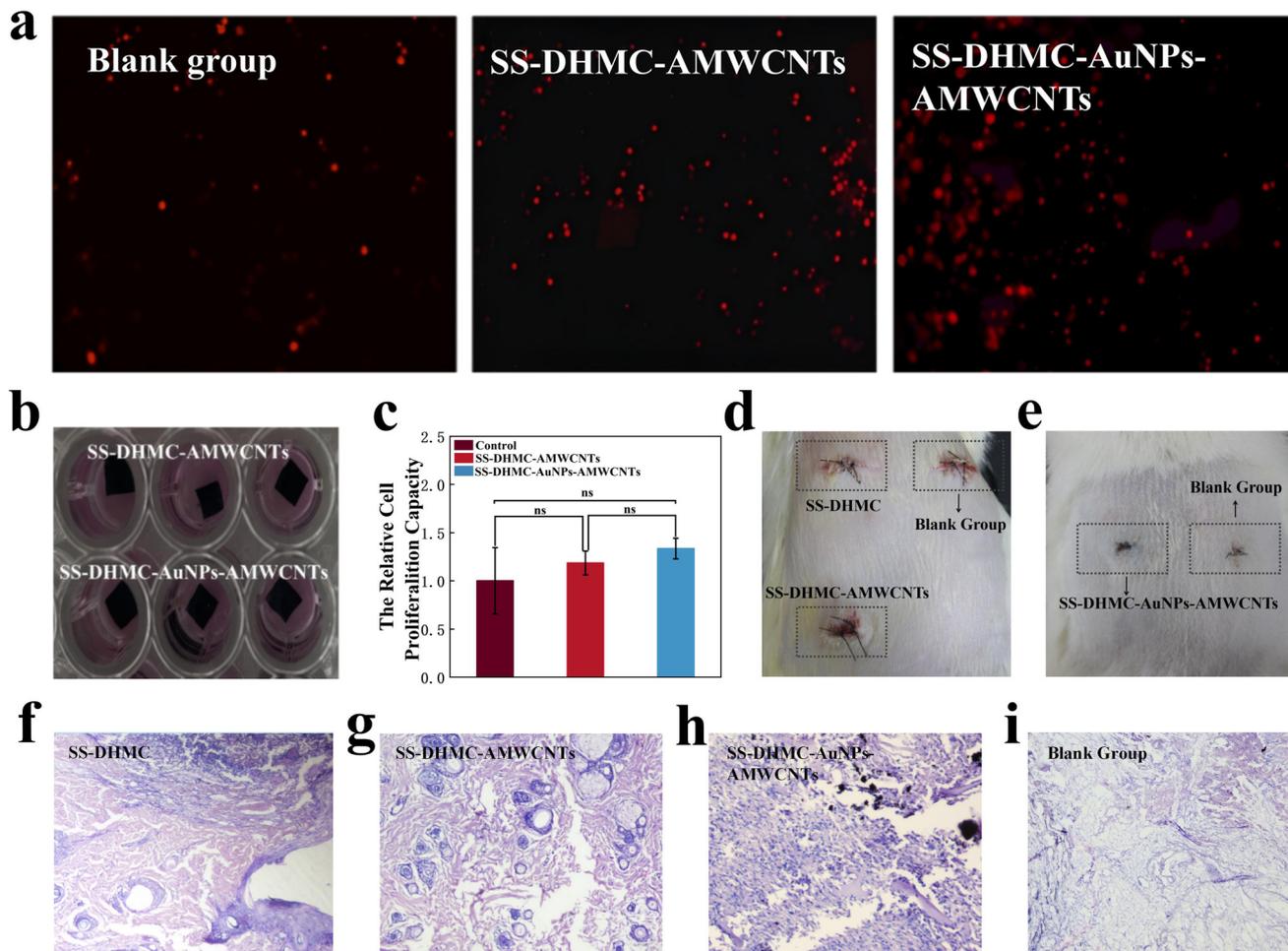
Fig. 3 Biocompatibility testing of SS–DHMC–AuNPs–AMWCNTs. (a) Fluorescence imaging of HeLa cells on a control surface and on SS–DHMC-AMWCNT and SS–DHMC–AuNPs–AMWCNT films; (b) representative images of CCK-8 assays measuring the proliferation of L929 cells in the presence of SS–DHMC–AMWCNT and SS–DHMC–AuNPs–AMWCNT films; (c) quantification of the CCK-8 assay as shown in panel (b), with data presented as mean $\pm$ SEM (n = 3); (d and e) representative images of three composite films subcutaneously implanted in rat dorsum; (f–i) H&E staining of subcutaneous tissues from rats implanted with SS–DHMC (f), SS–DHMC–AMWCNTs (g), SS–DHMC–AuNPs–AMWCNTs (h), and control materials (i).

samples were processed under endotoxin-minimizing conditions and sterilized prior to biological testing. At one week after implantation, no significant swelling or inflammatory exudation was observed in any treatment group (Fig. 3d and e). However, while rats implanted with SS–DHMC and SS–DHMC–AMWCNTs showed no obvious inflammatory responses (Fig. 3f, g and i), rats implanted with SS–DHMC–AuNPs–AMWCNTs exhibited mild localized inflammatory cell infiltration after one week (Fig. 3h). Histological analyses showed that the inflammatory cells primarily accumulated at the interface between the material and the tissue interface, as indicated by blue-stained regions in H&E staining, potentially due to mechanical stimulation from the rigid structure of the AMWCNTs and to the generation of trace reactive oxygen species that activated immune cells.[35] Importantly, this inflammatory response remained mild and within a physiological range that is normally observed upon biomaterial implantation.

The intent of the sensor is to be used for short-term (24 h) monitoring on the epidermis, which possesses an intact stratum corneum barrier and fewer immune cells compared to dermis.[36,37] Accordingly, our results suggest that the material demonstrates superior biocompatibility in epidermal applications. Human skin patch tests (Fig. S2) confirmed that the SS–DHMC–AuNPs–AMWCNT film caused no skin irritation or allergic reactions when applied for 48 h. Thus, the material performed comparably to commercial sterile dressings, thereby validating its safety for epidermal biosensing and supporting its clinical potential. The current *in vivo* assessment focused on short-term responses; longer-term degradation/eluate testing and surface-engineered variants will be evaluated in future work to further de-risk inflammatory responses for prolonged wear.

Kus-Liśkiewicz[38] proposed a series of *in vitro* and *in vivo* assays to be employed in the evaluation of the cytotoxicity and biocompatibility of gold nanoparticles (AuNPs); the SS–DHMC–

© 2026 The Author(s). Published by the Royal Society of Chemistry

AuNPs–AMWCNT composite demonstrates excellent biocompatibility in epidermal applications, meeting the biological requirements for biocompatibility. Compared with previously reported carbon-based nanocomposites,[39] this material shows significant advantages in biocompatibility. The biologically friendly interface constructed by the natural polymer matrix (SS–DHMC) provides an optimal microenvironment for cell growth,[40] while the uniform dispersion of nanomaterials achieved through process optimization avoids reactions caused by locally high concentrations of potential irritants.[41,42] The synergistic effects of these advantages endow the composite with reliable safety and stability, establishing a solid foundation for its application in medical monitoring tools. In future work, we plan to optimize the surface modifications of the AMWCNTs, such as introducing hydrophilic groups or biocompatible coatings, to more completely reduce potential inflammatory risks and expand its application potential in long-term implantable devices.

The mild, localized infiltration observed in the subcutaneous model should be interpreted in light of the sensor's short-term epidermal use, where the intact stratum corneum limits cellular exposure. To further reduce risk, future versions will apply anti-fouling surface modifications to the nanofillers (PEGylation or zwitterionic coatings; polydopamine-anchored hyaluronic acid/gelatin/sericin shells; thiolated-PEG end-capping on AuNPs) and mild oxidative/acid functionalization of CNTs to improve hydrophilicity. Antioxidant functional layers (e.g., polydopamine/tannic acid) will be explored to scavenge ROS near the interface. Regarding degradation, the SS–DHMC matrix is expected to yield peptides and cellulose-derived fragments, whereas metallic/carbonaceous fillers are largely insoluble; therefore, our follow-up will emphasize eluate testing (mass-loss/FTIR, ICP-MS for Au, CNT shedding by Raman), together with eluate cytotoxicity and macrophage cytokine assays to quantify inflammatory potential.

3.3 Electrochemical properties of SS–DHMC–AuNPs–AMWCNTs

3.3.1 Electrocatalytic mechanism and performance. We performed systematic electrochemical testing to investigate the glucose-sensing characteristics of the SS–DHMC–AuNPs–AMWCNT composite film. As shown in Fig. 4a, the sensing mechanism primarily relies on the functional synergy of two key components: AuNPs provide highly efficient catalytic active sites, while AMWCNTs construct a three-dimensional conductive network to ensure rapid electron transfer. During the catalytic process, the hydrated monolayer $[Au(OH)_{ads}]$ formed on the AuNP surface acts as an active center. It specifically interacts with the hydroxyl groups of glucose molecules, promoting the dissociation of hydrogen atoms at the anomeric carbon of glucose as protons while releasing electrons to generate gluconolactone.[14] The electrons produced by this oxidation process are rapidly transported to the electrode surface through the conductive pathway established by AMWCNTs, forming a detectable electrical signal.[43] Notably, AMWCNTs not only serve as an electron-

conducting medium but also significantly increase the loading capacity of active sites due to their large surface area.[44] Meanwhile, the hydrophilic nature of the SS–DHMC matrix facilitates glucose diffusion and mass transfer.[45,46] The synergistic interaction of these three components was established to collectively enhance the detection performance of the sensor.

Differential pulse voltammetry (DPV; Fig. 4b) revealed a distinct oxidation peak near 0.07 V for SS–DHMC–AuNPs–AMWCNTs, with a significantly higher current response compared to SS–DHMC and SS–DHMC–AMWCNTs, confirming the critical role of AuNPs in improving sensor sensitivity. Chronoamperometry (CA; Fig. 4c) further demonstrated that the SS–DHMC–AuNPs–AMWCNT composite film exhibited a substantially enhanced current response in glucose detection. This pronounced catalytic enhancement effect underscores the pivotal role of AuNPs in electrochemical glucose sensing, providing a strong foundation for developing other high-performance biosensors.

An electrochemical impedance spectroscopy (EIS) analysis based on the Randles equivalent circuit model[47–49] further elucidated the electron transfer properties at the material interface (Fig. 4d). The charge transfer resistance (R_{CT}) of SS–DHMC–AuNPs–AMWCNTs (537.8 Ω) was 24.2% lower than that of SS–DHMC–AMWCNTs (709.5 Ω). This kinetic result confirms that the high conductivity of AuNPs provides additional electron transfer pathways, while the synergistic interface formed with AMWCNTs reduces the interfacial energy barrier and promotes electron transfer.[50,51] An additional factor supporting the sensitivity of the detector is that the porous structure of the nanocomposite (Fig. 2c) contributes to an increased effective electrode area.

3.3.2 Kinetic analysis. Cyclic voltammetry (CV) provided important insights into the kinetic behavior of the material. SS–DHMC–AuNPs–AMWCNTs exhibited a significant enhancement of the redox peak current upon addition of 2 mM glucose, while control materials showed no such response (Fig. 4e), unequivocally confirming the catalytic role of AuNPs.[52] Furthermore, the CV profile of SS–DHMC–AuNPs–AMWCNTs progressively changed with increasing glucose concentration over a range from 0 to 14 mM (Fig. 4f), where both oxidation and reduction peak currents demonstrated linear relationships with glucose concentration (Fig. S3), indicating quantitative detection capability.

To elucidate the electrocatalytic mechanism of AuNPs in the oxidation of glucose, we systematically investigated the electrochemical behavior of SS–DHMC–AuNPs–AMWCNT-modified electrodes at varying scan rates (50–500 mV s^{-1}, Fig. 4g). The oxidation peak potential shifted positively while the reduction peak potential shifted negatively with increasing scan rates, characteristic of a quasi-reversible redox system.[53] Notably, the oxidation peak current showed strong linearity with the scan rate (Fig. S4), confirming a surface-adsorption-controlled process rather than a diffusion-controlled process.[54–56] This kinetic feature highlights the efficient catalytic activity of the surface sites of the AuNPs
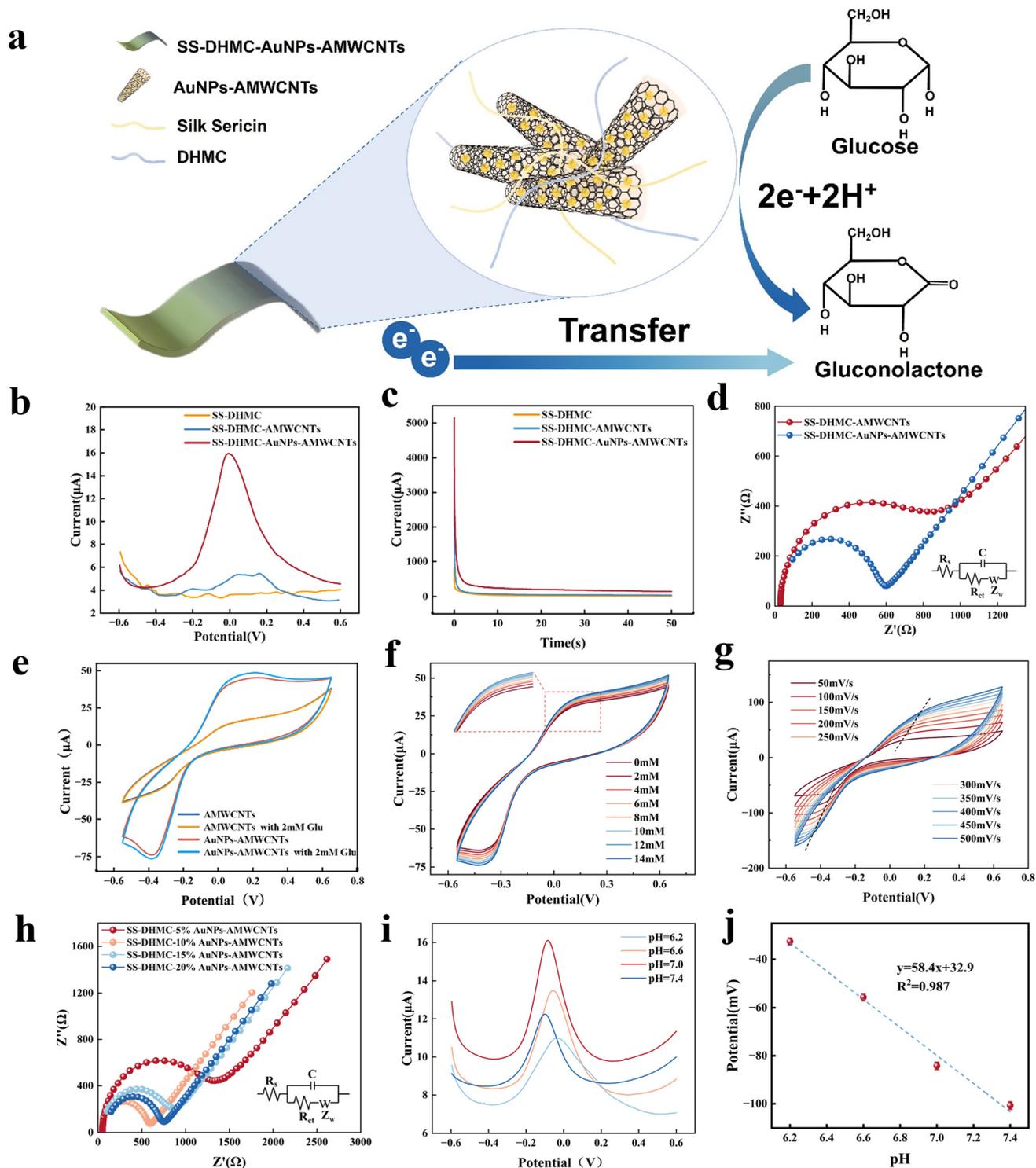
Fig. 4 Electrochemical performance and optimization of SS–DHMC–AuNPs–AMWCNTs. (a) Schematic illustration of glucose detection by the SS–DHMC–AuNPs–AMWCNT composite film; (b) DPV curves of SS–DHMC, SS–DHMC–AMWCNTs, and SS–DHMC–AuNPs–AMWCNTs in PBS; (c) CA responses of three composite films upon addition of 0.2 mM glucose in PBS (pH = 7.0); (d) Randles equivalent circuit models of SS–DHMC–AMWCNTs and SS–DHMC–AuNPs–AMWCNTs in 0.05 M KCl; (e) CV curves of SS–DHMC–AMWCNTs and SS–DHMC–AuNPs–AMWCNTs in PBS (pH = 7.0); (f) the CV images of SS–DHMC–AuNPs–AMWCNT films at different glucose concentrations; (g) the CV images of the SS–DHMC–AuNPs–AMWCNT film at different scanning speeds (50–500 mV); (h) Randles equivalent circuit models of SS–DHMC–AuNPs–AMWCNTs with different conductive filler contents in 0.05 M KCl; (i) DPV responses of the SS–DHMC–AuNPs–AMWCNT film at different pH values; (j) correlation between DPV peak potentials and pH values for the SS–DHMC–AuNPs–AMWCNT film, with data presented as mean ± SEM (n = 3).

and the facilitating exposure of active sites by the porosity of the composite.[57] The kinetic characteristics also suggest that the sensor response speed is unaffected by limitations of glucose diffusion and that sensitivity could be further enhanced through surface area optimization. The unique advantage of this study lies in achieving uniform dispersion of AuNPs and AMWCNTs within the flexible SS–DHMC network, maintaining high catalytic activity while preventing nanoparticle aggregation.[58,59]

3.3.3 Performance optimization and condition selection.
To optimize sensor performance, we systematically studied the effect of conductive filler content. An EIS analysis using the Randles equivalent circuit model (Fig. 4h) revealed a non-monotonic trend in R_{CT} (1259 Ω, 537.8 Ω, 697.3 Ω, and 605.5 Ω for 5%, 10%, 15%, and 20% filler content, respectively).[60] The 57.3% reduction in R_{CT} at 10% filler content can be attributed to two factors: (1) the enhanced electron transfer kinetics due to the catalytic activity of the AuNPs[61] and (2) improved charge transport *via* the 3D conductive network of the AMWCNTs. Beyond 10%, the performance declined due to pore blockage, which reduced the electrochemically active surface area,[62] consistent with the CV results showing optimal redox peaks at 10% filler (Fig. S5). The non-monotonic evolution of R_{CT} (minimum at 10%, increase at ≥15%) is characteristic of a percolation–porosity trade-off. Beyond the percolation optimum, excess AuNPs/AMWCNTs densify the filler network and partially block micro/mesopores, lowering the effective electroactive area and mass-transport. This is in line with the higher R_{CT} at ≥15% (Fig. 4h) and the reduced capacitive contribution in CV/DPV (Fig. S5). Consequently, 10% provides the best balance between catalytic-site density and accessible porosity.

The DPV response was measured over a pH range from 6.2 to 7.4 (Fig. 4i), and the shift in the oxidation peak potentials was found to correlate inversely with pH ($R^2 = 0.987$, Fig. 4j). The slope of the correlation line (58.4 mV pH^{-1}) was consistent with the theoretically ideal slope of a pH probe (59 mV pH^{-1}),[63,64] confirming that proton-coupled electron transfer occurred during glucose oxidation.[21]

Previous studies have reported that AuNPs can directly catalyze glucose oxidation to produce gluconic acid and hydrogen peroxide.[65] This catalytic process requires the participation of hydroxide ions (OH$^-$), in a similar manner to the catalytic activity of glucose oxidase (GOx). The pH-dependence observed for our system can be mechanistically explained as follows: under acidic conditions (pH < 7.0), insufficient hydroxyl groups are adsorbed on the surface of the gold, leading to limited catalytic activity. In contrast, under weakly basic conditions, the increased presence of hydroxide can lead to the formation of oxidized layers on the gold surfaces (*e.g.*, Au(OH)$_3$), which passivate the active sites and inhibit further glucose oxidation,[66] resulting in compromised oxidative capability. The optimal performance observed at neutral pH represents a balanced state where adequate OH$^-$ is available to participate in the reaction while excessive formation of gold oxides is prevented, thereby

ensuring both catalytic activity and material stability. This observation is consistent with previous reports demonstrating that gold electrodes exhibit maximum current response at neutral pH.[67]

In summary, the SS–DHMC–AuNPs–AMWCNT composite material achieves outstanding glucose sensing performance through rational structural design. The high sensitivity originates from the synergistic effect between the catalytic activity of AuNPs and the conductive network formed by AMWCNTs, while the porous structure ensures rapid mass transport and sufficient exposure of active sites. The confirmation of the importance of these parameters provides valuable insights into developing next-generation flexible biosensors.

3.4 Sensing performance of an SS–DHMC–AuNPs–AMWCNT electrode

3.4.1 Sensing characteristics and sensitivity.
The SS–DHMC–AuNPs–AMWCNT composite film exhibits an exceptional glucose sensing performance. DPV measurements (Fig. 5a and b) revealed linear responses to glucose over two concentration ranges (25–100 μM and 100–400 μM) with R^2 values of 0.9918 and 0.9975, respectively. The sensitivity of the detection was 13.43 and 5 μA mM^{-1} cm^{-2}, with a remarkably low limit of detection of 4 μM. Notably, this detection limit is substantially lower than the typical glucose concentration in sweat (10–200 μM),[68] suggesting that the detector meets practical requirements. The dual-linear characteristic reflects the changing mechanism of adsorption of glucose onto the surface of the AuNPs: abundant active sites ensure high sensitivity at low concentrations, while surface saturation leads to reduced sensitivity at higher concentrations.[69]

3.4.2 Selectivity for glucose and resistance to interference.
A comprehensive evaluation of selectivity was conducted by application of the sensor to detection of 0.2 mM glucose dissolved in 0.1 M PBS containing 2 mM concentrations of potential interferents (ascorbic acid, dopamine, KCl, NaCl, uric acid, urea, and lactic acid). The results of this analysis (Fig. 5c) revealed a signal deviation of less than 8%, with all responses within 99.6% to 107.6% of control. The relatively small variation can be attributed to (1) specificity in the catalytic activity of AuNPs,[70] (2) the charge-selective barrier effect of the SS–DHMC matrix,[71,72] and (3) the low oxidation potential of AuNPs.[73]

To further evaluate the glucose-specific recognition capability of our sensor, we determined its electrochemical responses to 2 mM concentrations of the compounds themselves, in the absence of glucose. As shown in Fig. 5d, when testing these interferents separately, the obtained peak currents were significantly lower than those obtained when measuring a solution containing 2 mM glucose. These findings confirm the sensor's specificity toward glucose detection, and they provide valuable mechanistic insights into the molecular recognition process to inform the design of other, highly selective non-enzymatic glucose sensors.
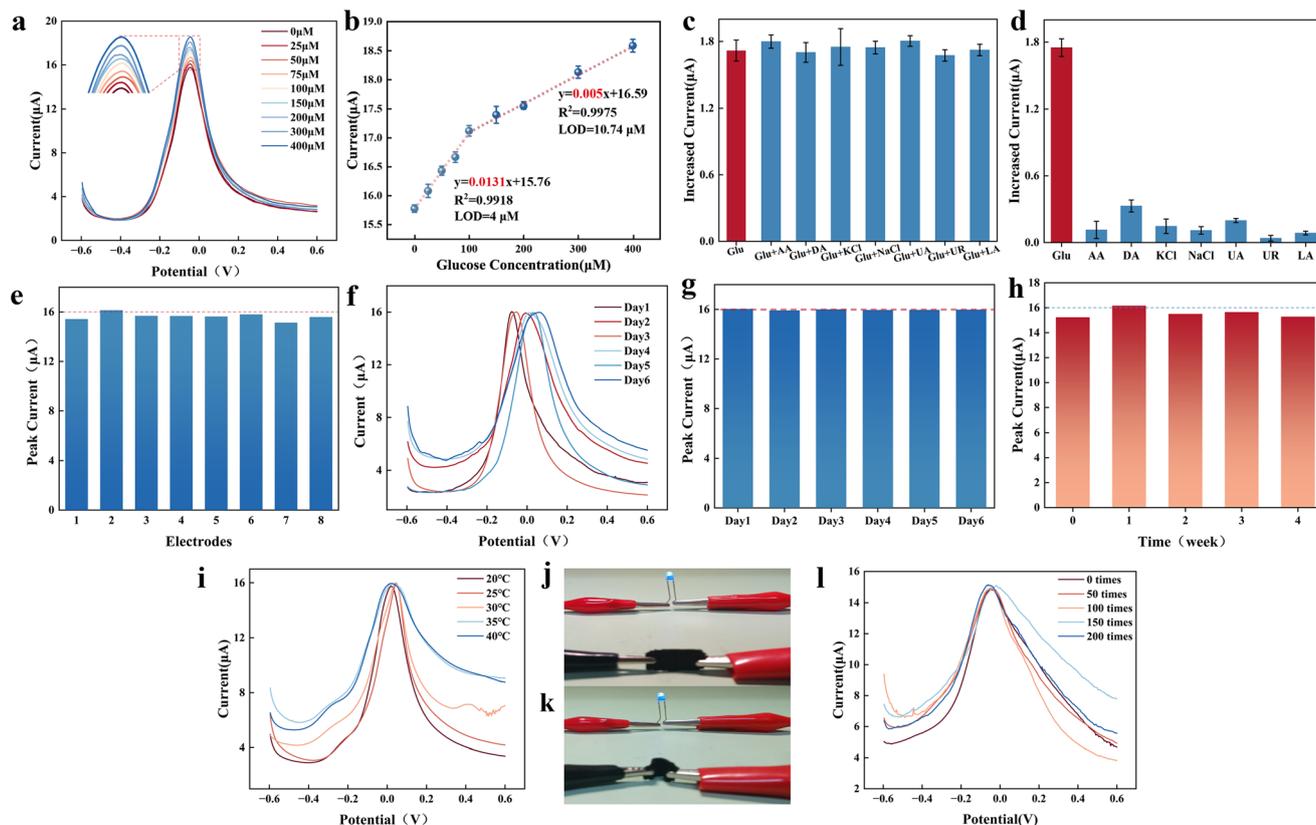
Fig. 5 Electrochemical sensing characteristics of SS–DHMC–AuNPs–AMWCNTs. (a) DPV responses of SS–DHMC–10%AuNPs–AMWCNTs at different glucose concentrations; (b) linear correlation between DPV peak current values and glucose concentrations (data presented as mean ± SEM, n = 3); (c) DPV responses of the SS–DHMC–AuNPs–AMWCNT film to 0.2 mM glucose and 2 mM concentrations of potentially interfering substances (data presented as mean ± SEM, n = 3); (d) DPV responses of the SS–DHMC–AuNPs–AMWCNT film to equal concentrations of glucose and other substances (data presented as mean ± SEM, n = 3); (e) reproducibility testing of eight identical SS–DHMC–AuNPs–AMWCNT films; (f) DPV result of the SS–DHMC–AuNPs–AMWCNT film stored for 6 d in PBS and then applied to the detection of 0.2 mM glucose; (g) peak current values from the data shown in (f); (h) peak current values from DPV analyses of the film stored for 4 weeks; (i) DPV performed at different temperatures; (j and k) conductivity performance evaluation of the SS–DHMC–AuNPs–AMWCNT film under flat (j) and folded (k) states (applied voltage: 10 V) using LED illumination; (l) DPV analyses of films folded to 180° multiple times.

As actual sweat contains much lower concentrations of the tested compounds than those analyzed here, and considering the limit of detection of 4 μM glucose, we concluded that the sensor exhibits sufficient performance for real-world applications. The high selectivity of the detector is particularly important for the prevention of false positive results emanating from exercise-induced fluctuations in metabolites (e.g., lactate) during dynamic monitoring.[74]

3.4.3 Stability and reproducibility. The practical application of a sensor requires that it remains stable over a sufficiently long period of time.[75] To evaluate the reliability and stability of our sensor, we conducted multi-level repeatability tests. Initial electrochemical testing of eight independently fabricated electrodes under identical conditions (0.1 M PBS, pH 7.0) revealed nearly identical glucose oxidation peak currents for all electrodes (Fig. 5e). This exceptional batch-to-batch reproducibility stems from our standardized fabrication process that ensures both material composition uniformity and homogeneous dispersion of AuNPs–AMWCNTs within the SS–DHMC matrix.

Long-term stability was assessed by (i) storage at 25 °C, ~70% RH for 1–4 weeks, (ii) continuous PBS (pH 7.0, 37 °C) immersion for 1–6 days, (iii) temperature cycling between 20–40 °C. The SS–DHMC–AuNPs–AMWCNT composite film maintained stable glucose oxidation peak currents after continuous immersion in PBS for 6 d (Fig. 5f and g). Subsequent monthly monitoring tests (Fig. 5h) demonstrated current response fluctuations within 7%, fully meeting the long-term stability requirements for wearable devices. These comprehensive stability validation experiments, conducted across multiple testing dimensions, conclusively demonstrate that the SS–DHMC–AuNPs–AMWCNT sensor possesses the reliability and stability necessary for practical implementation.

3.4.4 Mechanical properties and environmental adaptability. We considered that the temperature variations of human skin during physical activity[76] would potentially affect the performance of the sensor. DPV analyses (Fig. 5i) demonstrated that within the temperature range of 20 to 40 °C, which approximated skin temperature fluctuations during

exercise, changes to the current of the sensor in response to glucose remained negligible.

Furthermore, evaluation of the mechanical durability performance (Fig. 5j–l) showed that after 0/50/100/150/200 cycles of bending the sensor 180° (Fig. S7), the LED circuit brightness exhibited no significant change, indicating that the integrity of the conductive network was maintained. The lack of change of the DPV response current confirmed that the electrochemical active sites remained undamaged after repeated folding. These comprehensive tests verified the sensor's excellent environmental adaptability and mechanical stability under simulated usage conditions, meeting the stringent requirements for wearable health monitoring applications.

3.4.5 Comparison of sensor performance and application prospects. To contextualize our results within the landscape of noninvasive glucose sensing, we compared this work with representative wearable platforms (enzymatic and non-enzymatic; see Table S1). Our SS–DHMC–AuNPs–AMWCNT sensor achieves a LOD of 4 μM and a linear range of 25–400 μM at neutral pH (7.0), which spans the physiological sweat-glucose range. In contrast, many non-enzymatic Au-based sensors rely on alkaline electrolytes to boost catalysis, while enzymatic patches face enzyme instability and calibration drift. Here, the porous SS–DHMC matrix and AuNPs/AMWCNTs synergy deliver favorable sensitivity and selectivity under neutral conditions, together with mechanical durability (200 folding cycles). These features indicate competitive performance for practical, on-body monitoring, while larger clinical cohorts are planned to further substantiate generalizability.

In summary, the SS–DHMC–AuNPs–AMWCNT sensor achieves highly sensitive, selective, and stable glucose detection due to the design of the material and the optimization of its performance. The exceptional mechanical properties and environmental adaptability of this system make it an ideal candidate for wearable health monitoring. This work provides important ideas for non-enzymatic glucose sensor development while offering novel design concepts for flexible electronic devices.

3.5 *In vivo* deployment of wireless sweat glucose monitoring

3.5.1 Validation with artificial sweat and blood samples. Sweat is an ideal biofluid for noninvasive monitoring due to its ease of collection and its rich content of physiologically relevant biomarkers.[77] A correlation has been established between the concentrations of glucose in sweat and blood,[78] and the rapid secretion of sweat from highly vascularized sweat glands[79] enables reliable estimation of systemic glucose concentrations. Sweat glucose sensors thus hold great promise for continuous noninvasive diabetes monitoring.[80,81]

When applied in a simulated environment, the SS–DHMC–AuNPs–AMWCNT sensor demonstrated exceptional reliability. Three healthy adult volunteers (age 20–35 years; 2 males, 1 females) were recruited under informed consent. All experiments were performed in accordance with the

guidelines and approved by the Ethics Committee of Chongqing Medical University (Reference number: 2023011). Informed consents were obtained from human participants of this study. Application to artificial sweat yielded glucose recovery rates of 87.7 to 102.9% with RSD values of 1.3 to 2.6% (Table S2). Clinical validation using 10-fold diluted postprandial blood samples from the three volunteers showed recovery rates of 92.6 to 104.4%, with RSD values of 1.9 to 8.9% (Table S3), matching commercial glucometer readings. The slightly higher RSD values in blood testing reflect biological sample complexity, but the variability remained within acceptable limits. These results confirm the sensor's accuracy in physiological glucose detection and, combined with established sweat-blood glucose correlations,[78] demonstrate its potential for noninvasive glycemic monitoring.

3.5.2 Wearable real-time glucose monitoring system. We developed a noninvasive sweat glucose sensing system based on the SS–DHMC–AuNPs–AMWCNT material, integrating screen-printed electrodes with a portable electrochemical workstation for real-time detection (Fig. 6a). In human trials, healthy volunteers wore sensors during jogging. The same group of volunteers as in section 3.5.1 participated in this experiment. All experiments were performed in accordance with the guidelines and approved by the Ethics Committee of Chongqing Medical University (Reference number: 2023011). Informed consents were obtained from human participants of this study. The sensor measured glucose in the exercise-induced sweat, and blood glucose monitoring was performed in parallel using a commercial glucometer (GA-3 Sinocare, Fig. 6c). The system was also evaluated through pre-/post-prandial metabolic monitoring in which glucose levels were measured at 1-hour prior to a meal and at 0.5-, 2-, and 4-hours following a meal and through oral glucose tolerance testing (OGTT) after consumption of a standardized glucose solution (Fig. 6b and d). This human data demonstrates on-body feasibility and agreement with a commercial glucometer in healthy volunteers. Given the small sample size, results should be interpreted as proof-of-concept rather than population-level evidence.

Notably, no skin irritation or discomfort was reported by any of the volunteers, confirming the technology's safety and wearability. Agreement with the commercial glucometer was evaluated using Bland–Altman analysis (bias and 95% limits of agreement). A strong correlation ($R^2 = 0.981$) was observed between DPV current signals and glucometer readings (Fig. S6). Pre-/post-prandial monitoring (Fig. 6c) and OGTT (Fig. 6d) revealed a high correlation between sweat and blood glucose concentrations. This strong agreement can be attributed to the dynamic equilibrium between sweat glucose and blood glucose levels[82] and the close association between dermal interstitial fluid glucose and blood glucose.[83]

3.5.3 Prospects and challenges in clinical application. The developed SS–DHMC–AuNPs–AMWCNT sensor exhibited significant technical advantages in noninvasive glucose monitoring, with its enzyme-free catalytic mechanism providing
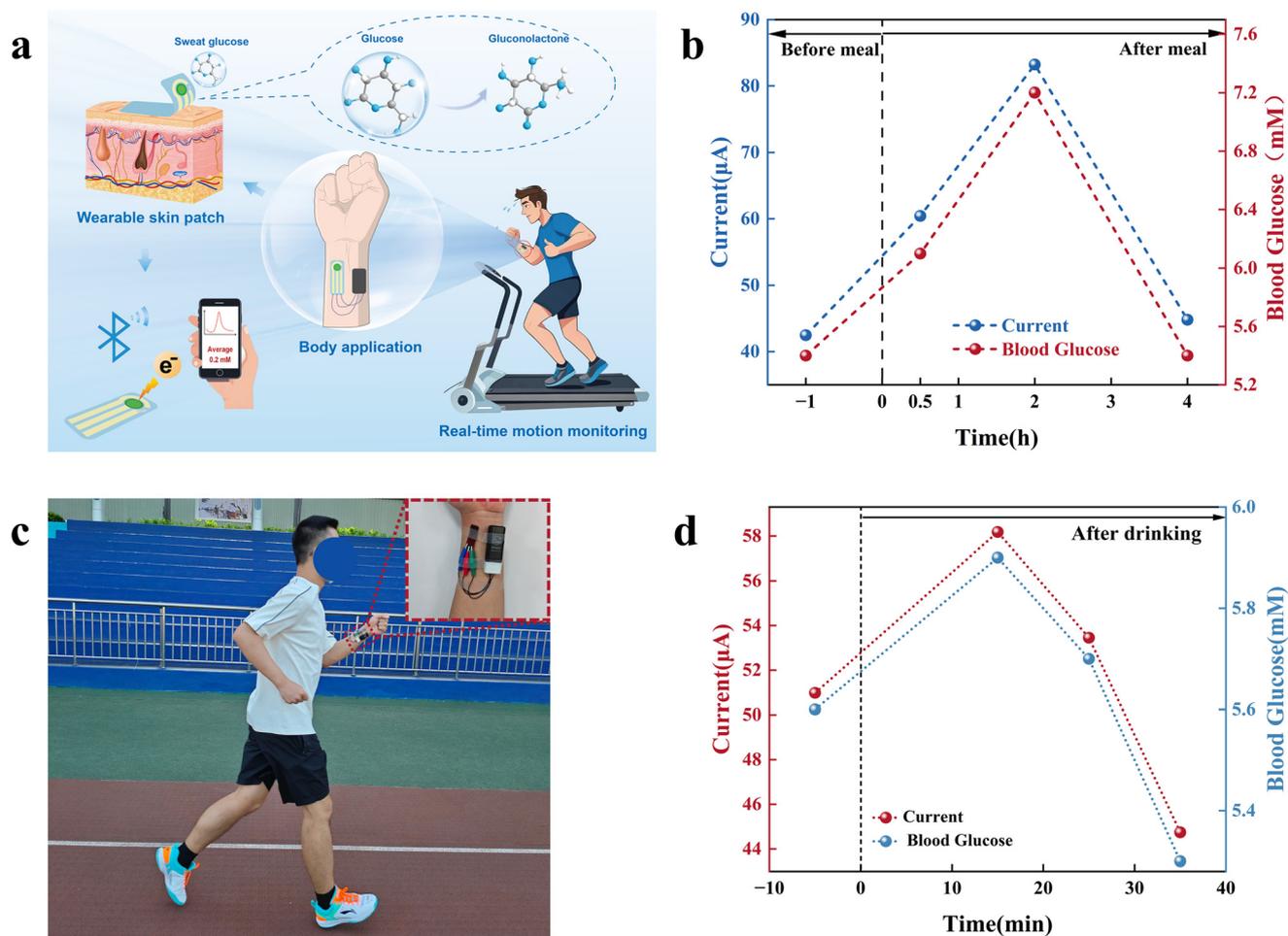
Fig. 6 *In vivo* application of wireless sweat glucose monitoring based on SS–DHMC–AuNPs–AMWCNTs. (a) Schematic diagram of the procedure for electrode usage in human subjects; (b) corresponding changes in sweat glucose-stimulated currents and traditionally monitored blood glucose levels before and after a meal; (c) wireless monitoring of glucose in forearm sweat from volunteers; (d) corresponding changes in sweat glucose-dependent currents and blood glucose levels before and after glucose solution consumption.

exceptional stability, the flexible patch design ensuring wearing comfort, and its high correlation with commercial glucometers validating detection reliability. However, several key technical bottlenecks must be addressed for clinical translation, including individual variations in sweat glucose baselines, cost considerations of precious metal conductive materials, and clinical validation in diabetic populations. Future applications will focus on algorithm optimization, refinement of the scaled-up production process, and establishment of diabetes monitoring databases to enhance system performance and reduce costs, thereby accelerating the transition from laboratory research to commercial implementation and providing innovative solutions for clinical needs such as diabetes management. In summary, the SS–DHMC–AuNPs–AMWCNT flexible sensor exhibits outstanding detection performance and clinical correlation in real-world applications. While sweat glucose monitoring still faces physiological challenges, this study confirms its practical value for noninvasive glycemic monitoring and offers a new technological option for medical applications including diabetes care. Large-scale clinical validation in future studies is warranted

to clarify its medical value and application prospects. The present study used a small healthy cohort and did not include participants with diabetes; therefore, clinical generalizability is limited. Future work will evaluate performance in a larger, diverse cohort including diabetic participants, incorporate subject-wise calibration to address inter-individual variability, and perform longitudinal assessments to establish robustness under pathological conditions.

4. Conclusion

In this study, we successfully transformed waste SS into high-performance flexible sensing material, leading to the development of a glucose sensor based on SS–DHMC–AuNPs–AMWCNTs with a demonstrated dual value in terms of both environmental and economic benefits. Through crosslinking reactions between SS and DHMC combined with synergistic modification strategies employing AuNPs and AMWCNTs, we significantly enhanced the material's mechanical properties and electrochemical activity while pioneering new applications for

natural polymers in wearable devices. The fabricated flexible sensor exhibits exceptional performance in noninvasive blood glucose monitoring, with strong correlation to commercial glucometers (R^2 = 0.981) confirming its clinical translation potential. This work not only provides a successful paradigm for high-value utilization of biological waste but also establishes a critical foundation for developing next-generation non-invasive health monitoring devices, showing broad application prospects in personalized medicine and chronic disease management. This work establishes a sustainable, flexible, enzyme-free sensing platform and demonstrates initial on-body feasibility; clinical validation in diabetic cohorts remains a necessary next step.

Author contributions

Xiaorui Huang: data curation, formal analysis, and writing – original draft. Yi Li: conceptualization, data curation, investigation, writing – review & editing. Boxiang Yang: data curation, visualization. Yuxuan Wu: data curation, and visualization. Zhuocheng Jiang: data curation and visualization. Jiuxi Sui: data curation and visualization. Siyi Xing: data curation and visualization. Xue Zhang: data curation and visualization. Hualin Lan: writing – review & editing. Hanyan Zou: conceptualization, data curation, investigation, writing – review & editing. Yuchan Zhang: conceptualization, data curation, funding acquisition, investigation, writing – review & editing. Guangchao Zang: conceptualization, data curation, funding acquisition, investigation, writing – review & editing.

Conflicts of interest

The authors declare no conflict of interest.

Data availability

Data will be made available upon request.

Supplementary information (SI): Fig. S1. The swelling rate of SS–DHMC–AuNPs–AMWCNTs film (n = 3). Fig. S2. Biocompatibility evaluation of SS–DHMC–AuNPs–AMWCNTs patch on human skin. Fig. S3. Relationship between redox peak currents and glucose concentration for SS–DHMC–AuNPs–AMWCNTs electrode. Fig. S4. Relationship between redox peak currents and scan rate for SS–DHMC–AuNPs–AMWCNTs electrode. Fig. S5. Cyclic voltammetry curves of SS–DHMC–AuNPs–AMWCNTs with varying contents of conductive fillers in PBS (pH 7.0). Fig. S6. Correlation analysis between non-invasive sweat glucose test results and commercial blood glucose meter measurements. Fig. S7. Flexible sensor folds 180 degrees. Fig. S8. (a) and (b) are the pre-fluid of SS–DHMC and SS–DHMC–AuNPs–AMWCNTs. (c) and (d) are the congealed SS–DHMC and SS–DHMC–AuNPs–AMWCNTs liquid after 24 hours. Table S1. Comparative analysis of detection performance between SS–DHMC–AuNPs–AMWCNTs and other non-enzymatic glucose sensors. Table S2. The detection of glucose in human sweat samples.

Table S3. The detection of glucose in human blood samples. See DOI: https://doi.org/10.1039/d5sd00188a.

References

1 J. Y. Xiao, *et al.*, Microfluidic Chip-Based Wearable Colorimetric Sensor for Simple and Facile Detection of Sweat Glucose, *Anal. Chem.*, 2019, **91**(23), 14803–14807.

2 Y. J. Lin, *et al.*, Porous Enzymatic Membrane for Nanotextured Glucose Sweat Sensors with High Stability toward Reliable Noninvasive Health Monitoring, *Adv. Funct. Mater.*, 2019, **29**(33), 1–8.

3 H. B. Lee, *et al.*, A wearable lab-on-a-patch platform with stretchable nanostructured biosensor for non-invasive immunodetection of biomarker in sweat, *Biosens. Bioelectron.*, 2020, **156**, 112133.

4 H. Guan, *et al.*, Processing Natural Wood into a High-Performance Flexible Pressure Sensor, *ACS Appl. Mater. Interfaces*, 2020, **12**(41), 46357–46365.

5 F. Wang, *et al.*, Transgenic PDGF-BB/sericin hydrogel supports for cell proliferation and osteogenic differentiation, *Biomater. Sci.*, 2020, **8**(2), 657–672.

6 M. C. Arango, *et al.*, Silk sericin as a biomaterial for tissue engineering: a review, *Int. J. Polym. Mater. Polym. Biomater.*, 2021, **70**(16), 1115–1129.

7 T. T. Cao and Y. Q. Zhang, Processing and characterization of silk sericin from Bombyx mori and its application in biomaterials and biomedicines, *Mater. Sci. Eng., C*, 2016, **61**, 940–952.

8 V. Bampidis, *et al.*, Safety and efficacy of hydroxypropyl methyl cellulose for all animal species, *EFSA J.*, 2020, **18**(7), 6214.

9 S. Koprivica, *et al.*, Regeneration of Aqueous Periodate Solutions by Ozone Treatment: A Sustainable Approach for Dialdehyde Cellulose Production, *ChemSusChem*, 2016, **9**(8), 825–833.

10 P. Wang, *et al.*, Cross-linking of dialdehyde carboxymethyl cellulose with silk sericin to reinforce sericin film for potential biomedical application, *Carbohydr. Polym.*, 2019, **212**, 403–411.

11 R. S. Singh and K. Chauhan, Immobilization of Inulinase on Aminated Multiwalled Carbon Nanotubes by Glutaraldehyde Cross-Linking for the Production of Fructose, *Catal. Lett.*, 2019, **149**(10), 2718–2727.

12 S. Alim, et al., Recent uses of carbon nanotubes & gold nanoparticles in electrochemistry with application in biosensing: A review, Biosens. Bioelectron., 2018, 121, 125–136.

13 M. S. Tamore, et al., Effect of functionalized multi-walled carbon nanotubes on physicomechanical properties of silicone rubber nanocomposites, J. Compos. Mater., 2019, 53(22), 3157–3168.

14 Y. Chen, et al., A wearable non-enzymatic sensor for continuous monitoring of glucose in human sweat, Talanta, 2024, 278, 126499.

15 J. E. Baio, D. J. Graham and D. G. Castner, Surface analysis tools for characterizing biological materials, Chem. Soc. Rev., 2020, 49(11), 3278–3296.

16 U. Kim, et al., Cellulose-chitosan beads crosslinked by dialdehyde cellulose, Nanomaterials, 2017, 24(10), 5517–5528.

17 P. Wang, et al., Cross-linking of dialdehyde carboxymethyl cellulose with silk sericin to reinforce sericin film for potential biomedical application, Carbohydr. Polym., 2019, 212, 403–411.

18 H. Tan, et al., Collagen cryogel cross-linked by naturally derived dialdehyde carboxymethyl cellulose, Carbohydr. Polym., 2015, 129, 17–24.

19 X. Li, et al., CNT/Sericin Conductive Nerve Guidance Conduit Promotes Functional Recovery of Transected Peripheral Nerve Injury in a Rat Model, ACS Appl. Mater. Interfaces, 2020, 12(33), 36860–36872.

20 F. A. Awadallah and S. Al-Muhtaseb, Carbon Nanoparticles-Decorated Carbon Nanotubes, Sci. Rep., 2020, 10(1), 4878.

21 Q. Peng, et al., Glucose determination behaviour of gold microspheres-electrodeposited carbon cloth flexible electrodes in neutral media, Anal. Chim. Acta, 2021, 1159, 338442.

22 R. Li, et al., Electrochemical biosensor based on the integration of maple leaf-like gold nanocrystal and truncated aptamer for detection of alpha-amanitin with high sensitivity, selectivity and rapidity, Food Chem., 2024, 453, 139639.

23 H. Yu, et al., Research Progress on Porous Carbon-Based Non-Precious Metal Electrocatalysts, Materials, 2023, 16(8), 3283.

24 D. Zhang, et al., Effect of porous structure on the electrochemical performance of FeS2 for lithium ion batteries, J. Nanosci. Nanotechnol., 2014, 14(8), 6095–6102.

25 X. Yang, et al., Monodisperse Carbon Nanospheres with Hierarchical Porous Structure as Electrode Material for Supercapacitor, Nanoscale Res. Lett., 2017, 12(1), 550.

26 X. He, Fundamental Perspectives on the Electrochemical Water Applications of Metal-Organic Frameworks, Nano-Micro Lett., 2023, 15(1), 148.

27 K. Jayaramulu, et al., Graphene-Based Metal-Organic Framework Hybrids for Applications in Catalysis, Environmental, and Energy Technologies, Chem. Rev., 2022, 122(24), 17241–17338.

28 K. Singh, K. K. Maurya and M. Malviya, Recent progress on nanomaterial-based electrochemical sensors for glucose detection in human body fluids, Microchim. Acta, 2025, 192(2), 110.

29 Y. P. Mo, et al., The intramolecular H-bonding effect on the growth and stability of Schiff-base surface covalent organic frameworks, Phys. Chem. Chem. Phys., 2016, 19(1), 539–543.

30 I. S. Kucherenko, et al., Advances in nanomaterial application in enzyme-based electrochemical biosensors: a review, Nanoscale Adv., 2019, 1(12), 4560–4577.

31 Y. Zhang, et al., Enzyme-catalyzed electrochemical aptasensor for ultrasensitive detection of soluble PD-L1 in breast cancer based on decorated covalent organic frameworks and carbon nanotubes, Anal. Chim. Acta, 2023, 1282, 341927.

32 L. Tang and W. Hu, Molecular determinants of biocompatibility, Expert Rev. Med. Devices, 2005, 2(4), 493–500.

33 V. Rosa, et al., Guidance on the assessment of biocompatibility of biomaterials: Fundamentals and testing considerations, Dent. Mater., 2024, 40(11), 1773–1785.

34 L. Zheng, et al., Engineering of Aerogel-Based Biomaterials for Biomedical Applications, Int. J. Nanomed., 2020, 15, 2363–2378.

35 J. Zhang, et al., Tumoral NOX4 recruits M2 tumor-associated macrophages via ROS/PI3K signaling-dependent various cytokine production to promote NSCLC growth, Redox Biol., 2019, 22, 101116.

36 S. de Szalay and P. W. Wertz, Protective Barriers Provided by the Epidermis, Int. J. Mol. Sci., 2023, 24(4), 3145.

37 P. R. Murphy, D. Narayanan and S. Kumari, Methods to Identify Immune Cells in Tissues With a Focus on Skin as a Model, Curr. Protoc., 2022, 2(7), e485.

38 M. Kus-Liśkiewicz, P. Fickers and I. Ben Tahar, Biocompatibility and Cytotoxicity of Gold Nanoparticles: Recent Advances in Methodologies and Regulations, Int. J. Mol. Sci., 2021, 22(20), 10952.

39 B. R. C. Menezes, et al., Recent advances in the use of carbon nanotubes as smart biomaterials, J. Mater. Chem. B, 2019, 7(9), 1343–1360.

40 X. Yang, et al., AR regulates porcine immature Sertoli cell growth via binding to RNF4 and miR-124a, Reprod. Domest. Anim., 2021, 56(3), 416–426.

41 D. R. Seshadri, et al., Flexible and Scalable Dry Conductive Elastomeric Nanocomposites for Surface Stimulation Applications, IEEE Trans. Biomed. Eng., 2023, 70(12), 3461–3468.

42 V. Castranova, P. A. Schulte and R. D. Zumwalde, Occupational nanosafety considerations for carbon nanotubes and carbon nanofibers, Acc. Chem. Res., 2013, 46(3), 642–649.

43 H. Z. Zhao, et al., Mechanisms for the direct electron transfer of cytochrome c induced by multi-walled carbon nanotubes, Sensors, 2012, 12(8), 10450–10462.

44 Y. Yang, et al., Flexible enzymatic biofuel cell based on 1, 4-naphthoquinone/MWCNT-Modified bio-anode and polyvinyl alcohol hydrogel electrolyte, Biosens. Bioelectron., 2022, 198, 113833.

45 X. Z. Zhang, D. Q. Wu and C. C. Chu, Synthesis, characterization and controlled drug release of thermosensitive IPN-PNIPAAm hydrogels, Biomaterials, 2004, 25(17), 3793–3805.

46 X. Chen, *et al.*, Terminal deoxynucleotidyl transferase induced activators to unlock the trans-cleavage of CRISPR/ Cpf 1 (TdT-IU-CRISPR/Cpf 1): An ultrasensitive biosensor for Dam MTase activity detection, *Biosens. Bioelectron.*, 2020, **163**, 112271.

47 H. Wang, *et al.*, Electrochemical impedance spectroscopy applied to microbial fuel cells: A review, *Front. Microbiol.*, 2022, **13**, 973501.

48 E. B. Bahadir and M. K. Sezginturk, A review on impedimetric biosensors, *Artif. Cells, Nanomed., Biotechnol.*, 2016, **44**(1), 248–262.

49 I. Turcan, *et al.*, Dielectrophoretic and Electrical Impedance Differentiation of Cancerous Cells Based on Biophysical Phenotype, *Biosensors*, 2021, **11**(10), 401.

50 J. Im, *et al.*, Functionalized Gold Nanoparticles with a Cohesion Enhancer for Robust Flexible Electrodes, *ACS Appl. Nano Mater.*, 2022, **5**(5), 6708–6716.

51 M. Mehrban, *et al.*, Fabrication of impedimetric sensor based on metallic nanoparticle for the determination of mesna anticancer drug, *Sci. Rep.*, 2023, **13**(1), 11381.

52 P. Pongsanon, *et al.*, Effect of Gold Nanoparticle Size on Regulated Catalytic Activity of Temperature-Responsive Polymer-Gold Nanoparticle Hybrid Microgels, *Gels*, 2024, **10**(6), 357.

53 S. Zhao, *et al.*, Glucose oxidase/colloidal gold nanoparticles immobilized in Nafion film on glassy carbon electrode: Direct electron transfer and electrocatalysis, *Bioelectrochemistry*, 2006, **69**(2), 158–163.

54 Y. Liu, *et al.*, MOF-polymer composites with well-distributed gold nanoparticles for visual monitoring of homocysteine, *Analyst*, 2024, **149**(5), 1658–1664.

55 W. Wang, *et al.*, Effects of Gold Nanospheres and Nanocubes on Amyloid-beta Peptide Fibrillation, *Langmuir*, 2019, **35**(6), 2334–2342.

56 H. Xiang, *et al.*, Au Nanozyme Driven Cascading Catalysis in Tollens' Reaction: An Insight of Glucose Oxidase-Like Mechanism, *Chemistry*, 2023, **29**(34), e202300454.

57 H. Zhangsun, *et al.*, NiCu nanoalloy embedded in N-doped porous carbon composite as superior electrochemical sensor for neonicotinoid determination, *Food Chem.*, 2022, **384**, 132607.

58 B. Liu, *et al.*, Highly-dispersed NiFe alloys in-situ anchored on outer surface of Co, N co-doped carbon nanotubes with enhanced stability for oxygen electrocatalysis, *J. Colloid Interface Sci.*, 2023, **635**, 208–220.

59 X. Cai, *et al.*, Molecular Mechanisms, Characterization Methods, and Utilities of Nanoparticle Biotransformation in Nanosafety Assessments, *Small*, 2020, **16**(36), e1907663.

60 Y. Chen, *et al.*, Advanced Metal-Organic Frameworks-Based Catalysts in Electrochemical Sensors, *Front. Chem.*, 2022, **10**, 881172.

61 I. Sarhid, *et al.*, Hexacyano Ferrate (III) Reduction by Electron Transfer Induced by Plasmonic Catalysis on Gold Nanoparticles, *Materials*, 2019, **12**(18), 3012.

62 M. H. Salehi, *et al.*, Electrically conductive biocompatible composite aerogel based on nanofibrillated template of bacterial cellulose/polyaniline/nano-clay, *Int. J. Biol. Macromol.*, 2021, **173**, 467–480.

63 W. Sun, *et al.*, Direct electrocatalytic oxidation of adenine and guanine on carbon ionic liquid electrode and the simultaneous determination, *Biosens. Bioelectron.*, 2008, **24**(4), 994–999.

64 C. S. Lee, S. H. Yu and T. H. Kim, One-Step Electrochemical Fabrication of Reduced Graphene Oxide/Gold Nanoparticles Nanocomposite-Modified Electrode for Simultaneous Detection of Dopamine, Ascorbic Acid, and Uric Acid, *Nanomaterials*, 2017, **8**(1), 17.

65 N. J. Lang, B. Liu and J. Liu, Characterization of glucose oxidation by gold nanoparticles using nanoceria, *J. Colloid Interface Sci.*, 2014, **428**, 78–83.

66 M. Pasta, F. Mantia and C. Yi, Mechanism of glucose electrochemical oxidation on gold surface, *Electrochim. Acta*, 2010, **55**(20), 5561–5568.

67 M. H. Hassan, *et al.*, Recent Advances in Enzymatic and Non-Enzymatic Electrochemical Glucose Sensing, *Sensors*, 2021, **21**(14), 4672.

68 D. R. Seshadri, *et al.*, Wearable sensors for monitoring the physiological and biochemical profile of the athlete, *npj Digit. Med.*, 2019, **2**, 72.

69 T. Kangkamano, *et al.*, Chitosan Cryogel with Embedded Gold Nanoparticles Decorated Multiwalled Carbon Nanotubes Modified Electrode for Highly Sensitive Flow Based Non-Enzymatic Glucose Sensor, *Sens. Actuators, B*, 2017, **246**(10), 854–863.

70 S. Hu, *et al.*, Enzyme-Free Tandem Reaction Strategy for Surface-Enhanced Raman Scattering Detection of Glucose by Using the Composite of Au Nanoparticles and Porphyrin-Based Metal-Organic Framework, *ACS Appl. Mater. Interfaces*, 2020, **12**(49), 55324–55330.

71 J. das Neves, R. Sverdlov and A. Sosnik, Molecular and cellular cues governing nanomaterial-mucosae interactions: from nanomedicine to nanotoxicology, *Chem. Soc. Rev.*, 2020, **49**(14), 5058–5100.

72 C. Kim, T. Kim and J. Cho, Selective Charge Carrier Transport and Bipolar Conduction in an Inorganic/Organic Bulk-Phase Composite: Optimization for Low-Temperature Thermoelectric Performance, *ACS Appl. Mater. Interfaces*, 2024, **16**(4), 5036–5049.

73 S. Y. Oh, *et al.*, Skin-Attachable, Stretchable Electrochemical Sweat Sensor for Glucose and pH Detection, *ACS Appl. Mater. Interfaces*, 2018, **10**(16), 13729–13740.

74 A. Philp, A. L. Macdonald and P. W. Watt, Lactate–a signal coordinating cell and systemic function, *J. Exp. Biol.*, 2005, **208**(Pt 24), 4561–4575.

75 A. Sonawane, P. Manickam and S. Bhansali, Stability of Enzymatic Biosensors for Wearable Applications, *IEEE Rev. Biomed. Eng.*, 2017, **10**, 174–186.

76 J. Liu, *et al.*, Graphene-Based Wearable Temperature Sensors: A Review, *Nanomaterials*, 2023, **13**(16), 110971.

77 A. M. V. Mohan, V. Rajendran, R. K. Mishra and M. Jayaraman, Recent advances and perspectives in sweat based wearable electrochemical sensors, *TrAC, Trends Anal. Chem.*, 2020, **131**, 116024.

78 H. Zafar, *et al.*, Comprehensive Review on Wearable Sweat-Glucose Sensors for Continuous Glucose Monitoring, *Sensors*, 2022, **22**(2), 638.

79 J. Moyer, *et al.*, Correlation between sweat glucose and blood glucose in subjects with diabetes, *Diabetes Technol. Ther.*, 2012, **14**(5), 398–402.

80 Z. Zhang, *et al.*, Sweat as a source of non-invasive biomarkers for clinical diagnosis: An overview, *Talanta*, 2024, **273**, 125865.

81 Q. Chen, *et al.*, Silk-Based Electrochemical Sensor for the Detection of Glucose in Sweat, *Biomacromolecules*, 2022, **23**(9), 3928–3935.

82 E. V. Karpova, E. E. Karyakina and A. A. Karyakin, Wearable non-invasive monitors of diabetes and hypoxia through continuous analysis of sweat, *Talanta*, 2020, **215**, 120922.

83 T. Saha, *et al.*, A Passive Perspiration Inspired Wearable Platform for Continuous Glucose Monitoring, *Adv. Sci.*, 2024, **11**(41), e2405518.